Phase-Compensated Optical Fiber-Based Ultrawideband Channel Sounder

Mbugua, Allan Wainaina; Fan, Wei; Olesen, Kim; Cai, Xuesong; Pedersen, Gert Frølund

Published in:
I E E E Transactions on Microwave Theory and Techniques

DOI (link to publication from Publisher):
10.1109/TMTT.2019.2948842

Publication date:
2020

Document Version
Accepted author manuscript, peer reviewed version

Phase-Compensated Optical Fiber-Based Ultrawideband Channel Sounder

Allan Wainaina Mbugua, Wei Fan, Kim Olesen, Xuesong Cai, and Gert Frølund Pedersen

***Abstract*— In this article, a novel vector network analyzer (VNA)-based ultrawideband (UWB) channel sounder using radio-over-fiber (RoF) techniques is presented. Benefiting from the usage of optical fiber cable, the measurement range and the dynamic range are significantly increased compared with the conventional coaxial-based VNA system. Specifically, using RoF increases the dynamic range to a maximum of 112 dB at 30 GHz for the back-to-back connection with an optical fiber cable of length 300 m. Moreover, a state-of-the-art phase compensation scheme using optical circulators is proposed for the first time. The novel scheme renders the channel sounder immune to stochastic phase changes in the optical fiber cable due to thermal changes and mechanical stress, thus permitting the remoting of virtual antenna arrays. The proposed channel sounder is experimentally validated in back-to-back measurements, an anechoic chamber, and practical indoor scenarios. The indoor channel measurements are conducted using a virtual uniform rectangular array (URA) at the millimeter-wave (mm-wave) band from 26.5 to 30 GHz. The measured results demonstrate the developed channel sounder's capability to perform UWB large-scale antenna array measurements with a long measurement range.**

***Index Terms*— Channel sounding, 5G, millimeter wave (mm-wave), radio propagation, radio-over-fiber (RoF), virtual antenna array.**

I. Introduction

THE dwindling spectrum resource at the sub-6-GHz bands has led to an upsurge in the recent research interest at millimeter-wave (mm-wave) bands, which will be the potential carrier frequencies for the fifth-generation (5G) cellular network [1]. The 5G cellular network is expected to offer 1000 times (1000×) increase in the aggregate data rate to what is currently offered in the fourth-generation (4G) cellular network [2]. To achieve this target, accurate channel characterization and modeling are fundamental for 5G system development and performance evaluation [3], [4]. This has subsequently led to the development of a plethora of channel sounders since the intricate nature of the radio channel makes it unfeasible to develop a channel sounder able to meet all sounding requirements [5].

Manuscript received May 14, 2019; accepted September 24, 2019. This work was supported in part by Huawei Technologies, in part by the Danish Council for Independent Research under Grant DFF611100525, and in part by the Virtusuo Project funded by Innovation Fund Denmark. *(Corresponding author: Wei Fan.)*

The authors are with the Antennas, Propagation and Millimetre-wave Systems (APMS) Section, Department of Electronic Systems, Faculty of Engineering and Science, Aalborg University, 9220 Aalborg, Denmark (e-mail: awm@es.aau.dk; wfa@es.aau.dk; ko@es.aau.dk; xuc@es.aau.dk; gfp@es.aau.dk).

Color versions of one or more of the figures in this article are available online at http://ieeexplore.ieee.org.

Digital Object Identifier 10.1109/TMTT.2019.2948842

Generally, the channel sounders reported in the literature are based either on time-domain or frequency-domain techniques [6]. The correlation-based channel sounders [7]–[12] are an example of time-domain-based systems. One of the techniques utilized in these sounders to extract the channel impulse response (CIR) is the transmission of pseudorandom noise (PN) sequences that are robust to noise [13]. For channel sounders working in the frequency domain, a frequency sweep over the band of interest is usually performed, and then, the CIR is obtained by an inverse discrete Fourier transform of the measured channel frequency response (CFR).

One of the most popular frequency-domain techniques has been the use of the vector network analyzer (VNA). The VNA has been widely used in static channel measurements due to its ability to perform a frequency sweep over a large bandwidth, ease of calibration, and low cost [14]–[17]. Nonetheless, channel sounding with the VNA suffers two major limitations. First, the channel must be kept static in the time duration of the frequency sweep. To obtain a higher signal-to-noise ratio (SNR), narrower intermediate frequency (IF) bandwidth settings are desirable that result in an increase in the frequency sweep time. For this reason, the VNA is constrained to channel sounding in the time-invariant channels [18], [19]. The second limitation is that the VNA setup requires a cable connection between the transmitter (Tx) and the receiver (Rx) to remote the antennas and for phase synchronization. Since the signal attenuation per unit length in coaxial cables increases with an increase in frequency [20], the measurement range is constrained to a few meters at mm-wave frequencies, while the system dynamic range is also reduced. Consequently, the VNA-based channel sounder has mainly been used for short-range deployment scenarios, e.g., indoor.

Several solutions to mitigate the signal loss in the coaxial cables in VNA-based channel sounders have been proposed in the literature. In [21]–[23], an low-noise amplifier (LNA) is added to the Rx chain, and a radio-frequency (RF) power amplifier is added to the Tx chain to improve the signal dynamic range. To minimize the signal loss in the RF chain and effectively increase the system dynamic range, a novel technique addressed in the literature is the application of the heterodyne principle. This involves the use of frequency upconverters close to the Tx antennas and downconverters at the Rx antennas. The transmission of a lower IF or a local oscillator (LO) signal in the coaxial cables results in a lower signal loss compared with transmitting the RF signal in the coaxial cables. For example, in [24], the Rx signal is downconverted to a lower IF signal that is transmitted

in the coaxial cables enabling the extension of the physical measurement range at mm-wave bands. In [25], the frequency sweep in the VNA is performed at a lower frequency, which is upconverted at the Tx for over-the-air transmission at 60 GHz and subsequently downconverted at the Rx. In channel measurements above 100 GHz, the VNA and the frequency extender modules are used [26], [27], which are based on the principle of upconversion and downconversion of the RF signal. In [28] and [29], signal loss in the coaxial cables is mitigated by transmitting the signal from a signal generator that is synchronized with a VNA, where the Rx signal is recorded.

To increase the VNA measurement range, an alternative solution is to exploit radio-over-fiber (RoF) techniques where the signal loss in the coaxial cables can be resolved by the use of electrical-to-optical (E/O) and optical-to-electrical (O/E) units and optical fiber cables [30]–[32]. The optical fiber transmission lines have the advantage of low signal loss, e.g., 0.4 dB/km for a single-mode optical fiber cable, which corresponds to 0.8 dB/km in the RF domain [33]. This is a significant improvement over the ultralow loss performance RF coaxial cables that can incur a signal loss, e.g., 1.59 dB/m at 30 GHz. Despite the low-loss properties of optical fiber cables, they are inherently sensitive to phase change due to the thermal and mechanical stresses [34], [35]. This implies that the RoF technique is not suitable for use in conjunction with virtual antenna arrays and has typically been used for power measurements [32]. This is a significant limitation since coherent and accurate phase measurements are pivotal to obtain the spatial profile of the multipath components (MPCs).

In [36], phase-coherent measurements are reported using RoF, where the LO signal is distributed to the downconverter and upconverter via optical fiber cables. Nonetheless, the phase correction details of the channel sounder are not reported. Similarly, the phase-coherent measurements are reported in [31] at 5.25 GHz and in [37] at 5 GHz with no details of the phase stability of the channel sounders. Moreover, the RF signal modulating the optical carrier in these cases is in the sub-6-GHz range where the phase errors due to the optical fiber could be small relative to the wavelength.

To enable phase-coherent long-range channel sounding measurements for ultrawideband (UWB) systems with the VNA using RoF techniques, two phase correction strategies were proposed and discussed briefly by Fan *et al.* [38]. The bidirectional scheme was shown to be effective in mitigating the phase change due to thermal and mechanical stresses. In this article, the principle of the method introduced in [38] will be further explained with both theoretical analysis and experimental validations. The optical carrier is modulated by an RF signal both in the sub-6-GHz range and the mm-wave frequency range. A novel phase-compensation mechanism is implemented using two three-port optical circulators. The underlying concept of this novel technique is to have bidirectional signal transfer on the same optical fiber cable where the signal to the Tx antenna is fed back to the VNA. Using the feedback signal, the impairments that are introduced by the optical fiber cable can then be deembedded from the channel measurements. In addition to the phase compensation, a dynamic range of 112 dB is attained for the back-to-back setup due to the significant reduction of signal loss as a result of the RoF technique. To the best of our knowledge, this is the first of a kind of VNA-based channel sounder employing the novel phase-compensation mechanism using optical circulators.

The rest of this article is organized as follows. Section II outlines the channel sounder's architecture, Section III contains the details of the validation measurements, Section IV outlines the measurement campaigns in realistic propagation environments, and finally, Section V concludes this article.

II. Channel Sounder Architecture

The heart of the channel sounder shown in Fig. 1 is the VNA with the capability of performing a frequency sweep from 10 MHz to 67 GHz. An optical fiber link with a frequency range of 1 to 50 GHz is used for remoting the Tx antenna. The optical fiber link is composed of a Tx, which is an externally modulated laser with a center wavelength of 1550 nm and two Rxs (photodetector), one for the forward link and the other for the feedback link, as shown in Fig. 2. The optical fiber link has preamplification and postamplification stages with a gain that varies from 12 dB at 1 GHz to -18 dB at 50 GHz at room temperature. The optical fiber link has a noise figure of 11 dB at 1 GHz and the maximum is 31 dB at 45 GHz. However, the noise figure is relatively flat with a value of 18 dB in the frequency band between 25 and 30 GHz.

A one-to-two optical power splitter is used to divide equally the optical power between the forward and feedback links, which results in an RF power loss of 6 dB at each port. Two nonpolarization-maintaining three-port optical circulators are used to enable bidirectional signal transmission on the same single-mode optical cable of length 300 m. The bidirectional signal transmission on the same optical fiber cable is attained by exploiting the nonreciprocity property of the optical circulators that have a peak isolation of 40 dB between port T and port R, as shown in Fig. 1, and thus, the signals in the forward and feedback links are sufficiently isolated. The nonpolarization-maintaining optical circulators enable the use of a nonpolarization-maintaining single-mode optical fiber cable, which is less expensive and has lower attenuation compared with a polarization-maintaining optical fiber cable. An RF amplifier with a frequency range of 26.5–40 GHz, a gain of 40 dB, a noise figure of 6.2 dB, and a 1-dB compression point of 20 dBm is used after the O/E stage before the signal is fed to the Tx antenna. A suitable heat sink is added to maintain the thermal stability of the RF amplifier, as shown in Fig. 2. The cascade of the amplification by the optical fiber link and the RF amplifier results in a total noise figure of 18.3 dB at 30 GHz. The channel sounder's components are outlined in Table I.

A. Principle of Operation

In VNA-based channel measurements, the radio channel is considered the device under test (DUT), and the CFR can then be obtained from the measured scattering parameter (S-parameter). In conventional coaxial-based VNA-based systems, a normalization procedure is usually carried out to

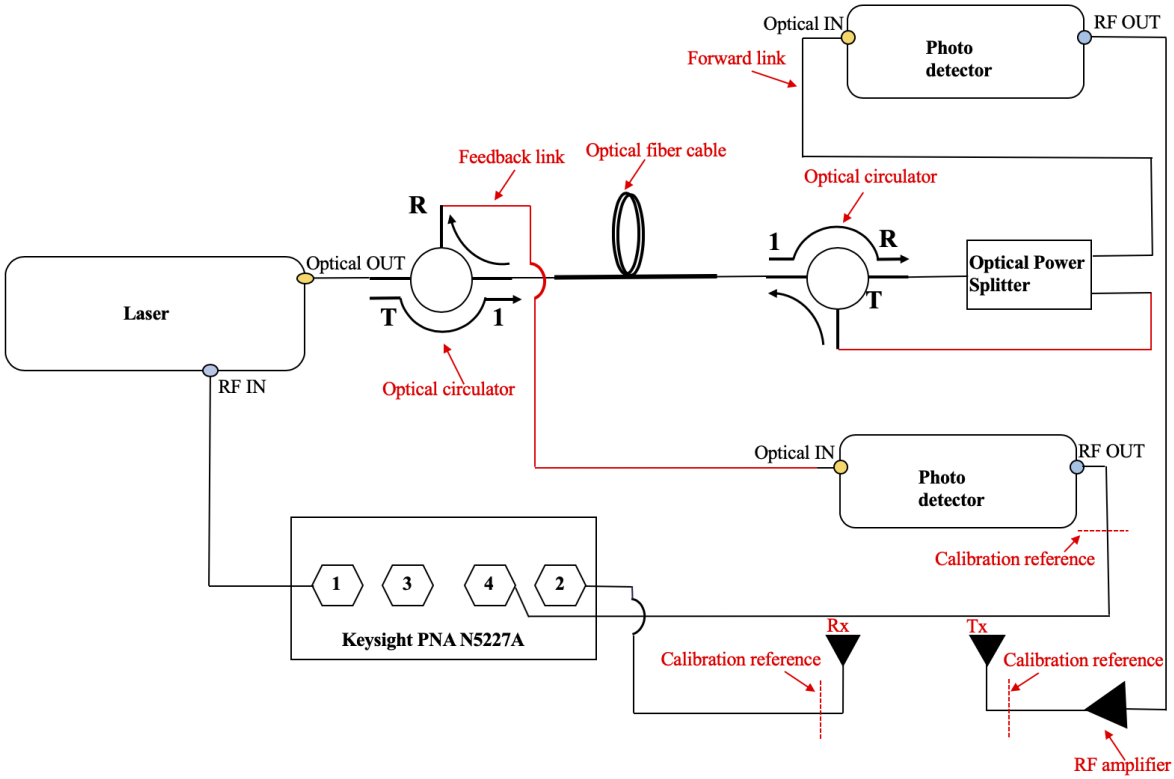

Fig. 1. Block diagram of the proposed RoF VNA-based channel sounder.

TABLE I
CHANNEL SOUNDER'S COMPONENTS

Part	Name	Frequency/ Wavelength
VNA	Keysight PNA N5227A	10 MHz to 67 GHz
Optical power splitter	JDS Uniphase FFC-CKH12B105-003	1550 nm
RF amplifier	Cernex CBM26402520	26.5 GHz to 40 GHz
RF attenuator	Pasternack PE7090-20	DC to 40 GHz
Laser	Linear Photonics QMOD XMTQ-C-A-24	1550 nm
Photo detector	Linear Photonics QMOD XMRQ-C-A-24	1550 nm
Optical circulator	OZ optics FOC-12N-111-9/125-SSS-1550-55-SCASCASCA-1-1	1550 nm

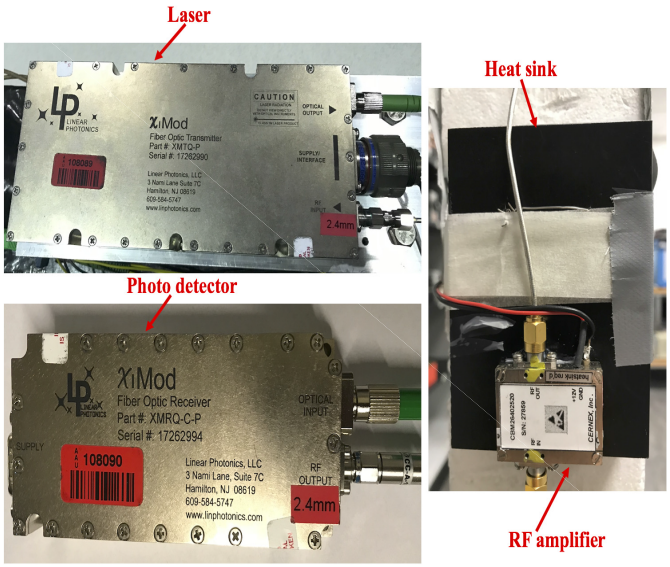

Fig. 2. Photograph of the laser, the photodetector, and the RF amplifier with the heat sink mounted.

deembed the frequency response of the cables. The basic assumption behind the normalization procedure is that the frequency response of the cables is time-invariant. However, when using the optical fiber cables subtle changes in temperature and mechanical stress can cause a significant phase variation, which results in a large deviation from normalization. This can result in significant errors in the measured CFR. To mitigate these errors, a feedback link is necessary to record the signal drift caused by the optical fiber cable. Optical circulators enable bidirectional signal transmission on the same optical fiber cable, and hence, the forward link and the feedback link can use the same cable, as shown in Fig. 1.

The forward and feedback links are recorded in the VNA as the S-parameters $S_{21}(f)$ and $S_{41}(f)$, respectively. After normalization in the back-to-back setup, the frequency response of the forward ($S_{21}(f)$) and feedback ($S_{41}(f)$) links are both equal to one. Replacing the back-to-back connection with suitable antennas, the CFR, $H(f)$ can be recorded in

$S_{21}(f)$ as

$$S_{21}(f) = 1 \cdot H_{\text{fw}}(f) \cdot H(f). \tag{1}$$

The error term $H_{\text{fw}}(f)$ is due to the mechanical stress and thermal changes on the optical fiber cable. Similarly, for the feedback link, the error term $H_{\text{fb}}(f)$ is embedded in the measured S-parameter $S_{41}(f)$ as

$$S_{41}(f) = 1 \cdot H_{\text{fb}}(f). \tag{2}$$

The bidirectional signal transfer on the same cable implies that the signal in the feedback link has undergone twice the phase change in the forward link due to mechanical stress and thermal changes on the optical fiber cable. The frequency response $H_{\text{fb}}(f)$ can thus be written as

$$H_{\text{fb}}(f) = H_{\text{fw}}^2(f). \tag{3}$$

In practical VNA measurements, the phase of the complex frequency responses $S_{21}(f)$ and $S_{41}(f)$ are usually wrapped, e.g., in the interval $[-\pi, +\pi]$ radians. The phase β_{41} of the complex frequency response $S_{41}(f)$ is unwrapped to obtain ϕ_{41}. The unwrapped phase ϕ_{41} is divided by 2 and wrapped back to the interval $[-\pi, +\pi]$ radians to obtain ψ_{41}. Consequently, the error term $H_{\text{fw}}(f)$ can be deembedded from the CFR $H(f)$ as follows:

$$H(f) = \frac{S_{21}(f)}{\sqrt{|S_{41}(f)|}e^{j\psi_{41}}}. \tag{4}$$

B. Link Budget

The system link budget at 30 GHz for the back-to-back connection is shown in Fig. 3. The VNA Tx power is set to -12 dBm, which gives a safe margin of 1 dB from the 1-dB compression point of the laser. After the E/O conversion stage, the optical signal for the forward link and the feedback link is isolated from each other using a pair of optical circulators. The optical circulators have an associated insertion loss that results in a total RF signal penalty of 4.3 dB. On the other hand, the optical power splitter causes an RF power degradation of 6 dB. Thus, the phase compensation comes at a cost of approximately 10.3-dB signal loss for the forward link.

The power at the output of the O/E stage is -30 dBm, which is not sufficient for channel sounding purposes, particularly at the mm-wave band where the free-space loss is quite high. An RF amplifier with a 40-dB gain is employed, which boosts the signal power to 9.8 dBm. In the Rx chain, the 0.1-dB Rx compression at test port 2 of the VNA is 10 dBm. To avoid driving the Rx at test port 2 into compression, an RF attenuator of 20 dB is used during the calibration process and later deembedded in postprocessing. The obtained dynamic range is thus 112 dB for the back-to-back connection at 30 GHz. Note that the noise floor of the VNA is specified for an IF bandwidth of 10 Hz and is subject to the change depending on the IF bandwidth setting.

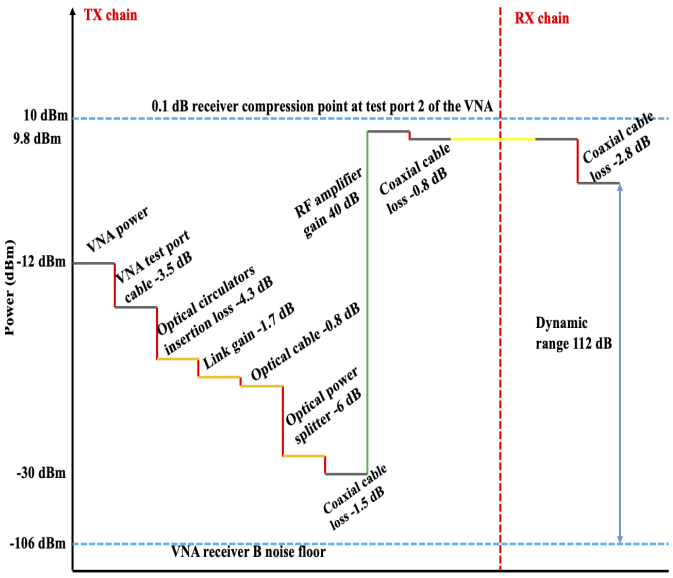

Fig. 3. Link budget of the channel sounder at 30 GHz.

III. Channel Sounder Validation

The channel sounder is validated using back-to-back measurements and the over-the-air tests using omnidirectional antennas in an anechoic chamber. The purpose of the back-to-back test is to test the amplitude and phase stability under the following two scenarios:

1) cable bending/mechanical stress;
2) thermal change/signal drift over time.

Amplitude and phase stability are fundamental if the channel sounder is to faithfully record the characteristics of the channel. Instability in the amplitude can lead to a false impression of frequency selective fading in a channel [39], whereas the phase instability leads to errors in the angle-of-arrival (AoA) estimation when using virtual antenna arrays. On the other hand, the over-the-air tests in the anechoic chamber are used to validate the whole measurement system, including the Tx and Rx antennas.

A. Cable Bending

In practical virtual antenna array measurements, mechanical stress on the optical fiber cable is inevitable due to the movement of the antenna positioning stages. To characterize the cable bending, the optical fiber cable is mounted on the turntable used for virtual uniform circular array (UCA) measurements, as shown in Fig. 4. The turntable with a radius of 0.5 m is rotated 720 steps to make a virtual circle where each step corresponds to a 0.5° movement in the virtual circle. For example, when the rotating arm is at the 60th step, as shown in Fig. 4, this corresponds to a 30° movement in the virtual circle. In this way, different cable bending effects that would be experienced in practical virtual UCA measurements are mimicked, and the frequency response is recorded at each step. In this case, the system is modified to exclude the RF amplifier shown in Fig. 1 to allow the characterization of the phase characteristic of the optical fiber link from 1 to 30 GHz. The phase is then measured at the

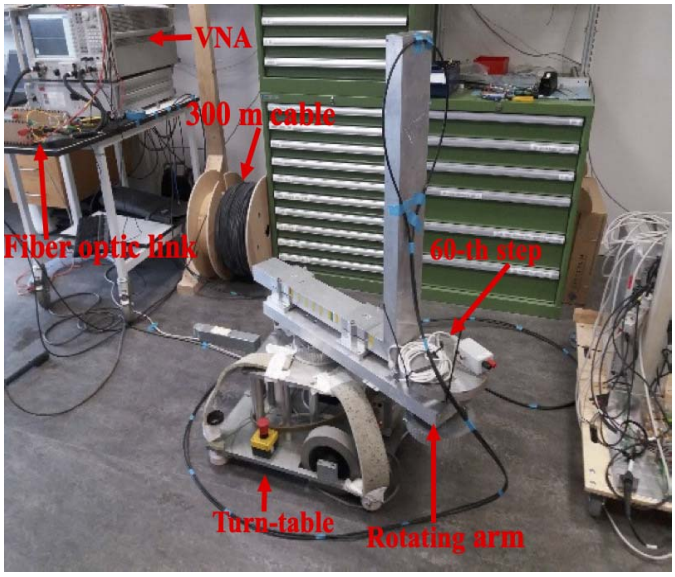

Fig. 4. Mechanical bending of the optical fiber cable using a turntable used for virtual array measurements. The rotating arm is at the 60th step of the virtual circle, which corresponds to 30° in the virtual UCA.

calibration reference, as shown in Fig. 1. Note that before the measurement, an initial normalization procedure is carried out for the back-to-back connection. This effectively shifts the phase reference plane from the VNA ports to the calibration reference plane, as shown in Fig. 1.

Mechanical stress essentially results in a change of the effective length of the optical fiber cable. The change in the effective length of the optical fiber cable results in a phase change that is directly proportional to the frequency. This can be observed in Fig. 5, where the lower frequencies experience a smaller phase change compared with the higher frequencies, as the turntable moves along the 720 points of a circle. The gradient of the linear phase response varies at every step of the turntable, meaning that at each step, the effective length of the optical fiber cable is different. Since the bending of the optical fiber cable is rather stochastic, its effective length at different steps is also random, as shown in Fig. 5. Nonetheless, the phase change at each step for the forward link in Fig. 5(a) is observed to be half that of the feedback link in Fig. 5(b) at each frequency point from 1 to 30 GHz. After the phase compensation, the phase deviation due to cable bending is maintained within 2.5° at 30 GHz, as shown in Fig. 5(c).

B. Signal Drifting Over Long Measurement Time

Signal drift over long measurement time is highly likely in practical measurement due to the thermal drift of the measurement system and in particular the optical fiber cable. Virtual antenna array measurements involving large-scale elements (i.e., measurements over many spatial points) can span several hours to record one channel snapshot. Besides keeping the channel static, it is also crucial that the measurement system has no signal drift or the signal drift is insignificant during the entire measurement period. However, the subtle changes in the ambient temperature have been reported in the literature to cause a significant phase change of the signal propagating

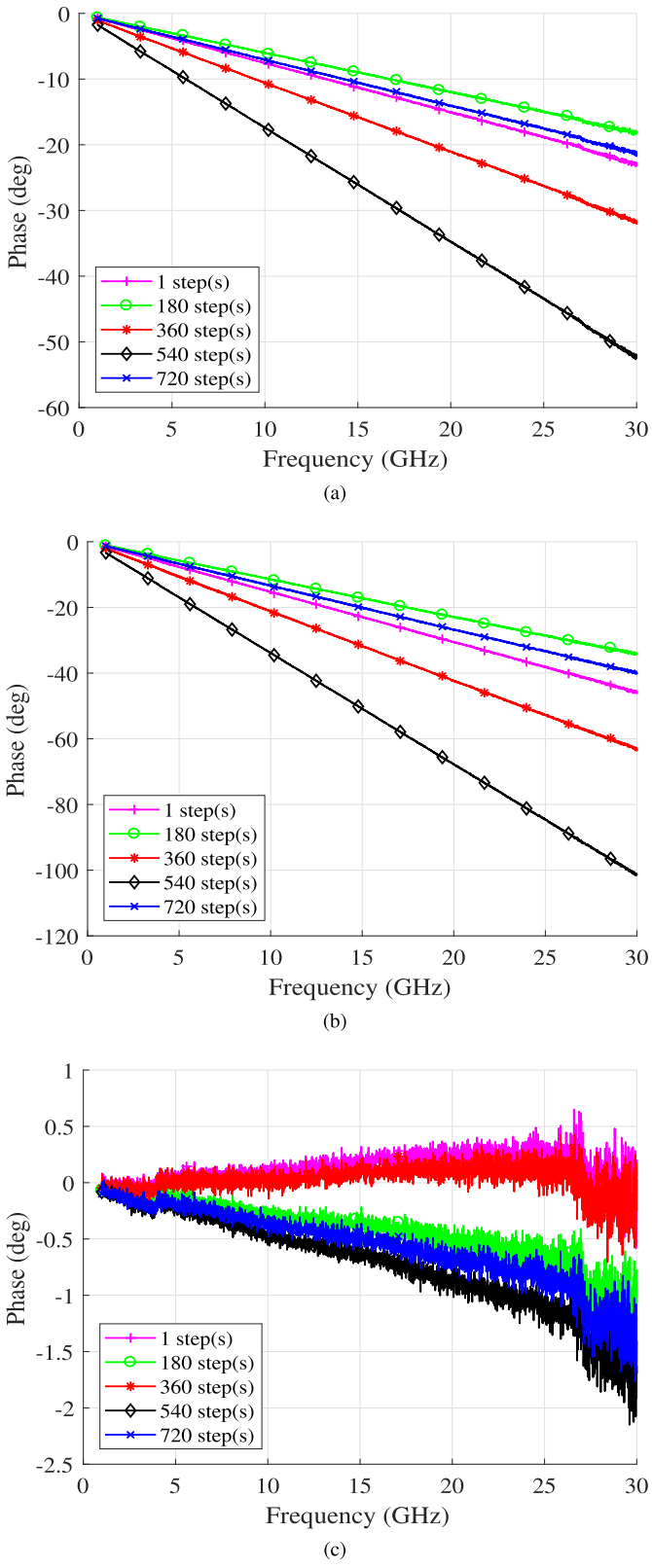

Fig. 5. Unwrapped phase of the channel sounder with cable bending. (a) Phase of the forward link. (b) Phase of the feedback link. (c) Compensated phase.

in the optical fiber cable [34], [35]. To verify the robustness of the system to the phase change on the optical fiber cable due to an ambient temperature change, the back-to-back measurement

using the circuit in Fig. 1 is carried out. A 20-dB attenuator is included in the back-to-back setup to keep the signal level into the VNA Rx at test port 2 below the 0.1-dB compression point. The VNA and the RF amplifier are turned on for at least 30 min before a normalization procedure is carried out for both the forward and feedback links. A frequency sweep is then performed continuously for a period of 17 h, during which the data are saved every 5 min due to data storage constraints. During this period, the channel sounder is kept stationary in a secured room to ensure no movement on the optical fiber cable occurred due to personnel. The room has standard air conditioners to maintain the ambient temperature at a predefined level. Nonetheless, a variation of more than 1 °C would occur, mainly due to the heat generated by the VNA over the long measurement period, which can cause significant phase change on the 300-m-long optical cable [34], [35].

The phase of the channel sounder with the RF amplifier is shown in Fig. 6. In the forward link, the phase can be observed to vary over 50° at 30 GHz, as shown in Fig. 6(a). In the feedback link, the phase change can be seen to be twice that in the forward link, as shown in Fig. 6(b). The phase compensation is then performed using (4). The compensated phase for a period of 17 h can be seen to be maintained within 2.5° at 30 GHz, as shown in Fig. 6(c). This demonstrates the robustness of the phase compensation mechanism using the optical circulators.

The amplitude which is computed as the absolute square of the frequency response is shown in Fig. 7. The amplitude varies by approximately 0.2 dB for the measurement in the first 30 min. After 30 min, the amplitude stabilizes and the variation is less than 0.1 dB for the next 16 h and 30 min. Overall, the amplitude of the system was observed to be very stable, as shown in Fig. 7.

C. Anechoic Chamber Measurements

To evaluate the system, the over-the-air measurements are carried out in an anechoic chamber, as shown in Fig. 8. At the Tx and the Rx, vertically polarized biconical antennas with omnidirectional radiation patterns in the azimuth are employed. The Tx antenna has an operation frequency of 1.5–40 GHz [40], whereas the Rx antenna *(AINFO-SZ-2003000/P)* has an operation frequency of 2–30 GHz. A virtual uniform rectangular array (URA) made of 900 virtual antenna elements (i.e., 30 × 30) with an interelement spacing of 0.4λ at 30 GHz is implemented at the Tx by moving the Tx antenna along the predefined positions in space. The movement of the Tx antenna is optimized to reduce measurement time by moving along the x-axis for a fixed position of the y-axis. At the end of the x-axis, the antenna positioning stages shift to the next y-axis position and reverse along the x-axis. This process is repeated until all the positions in space are covered to create the virtual URA, which takes a total of 2 h. A summary of the measurement parameters is outlined in Table II.

In the anechoic chamber measurements, the Tx and Rx antennas are separated by 212 cm. In an ideal situation, the propagation channel should consist only of the line-of-sight (LOS) path. However, this is not the case due to imperfection in the chamber and reflections from the measurement equipment. Nonetheless, the power level of the reflections is 30 dB below the LOS component as shown in the power angle delay profile (PADP) in Fig. 9.

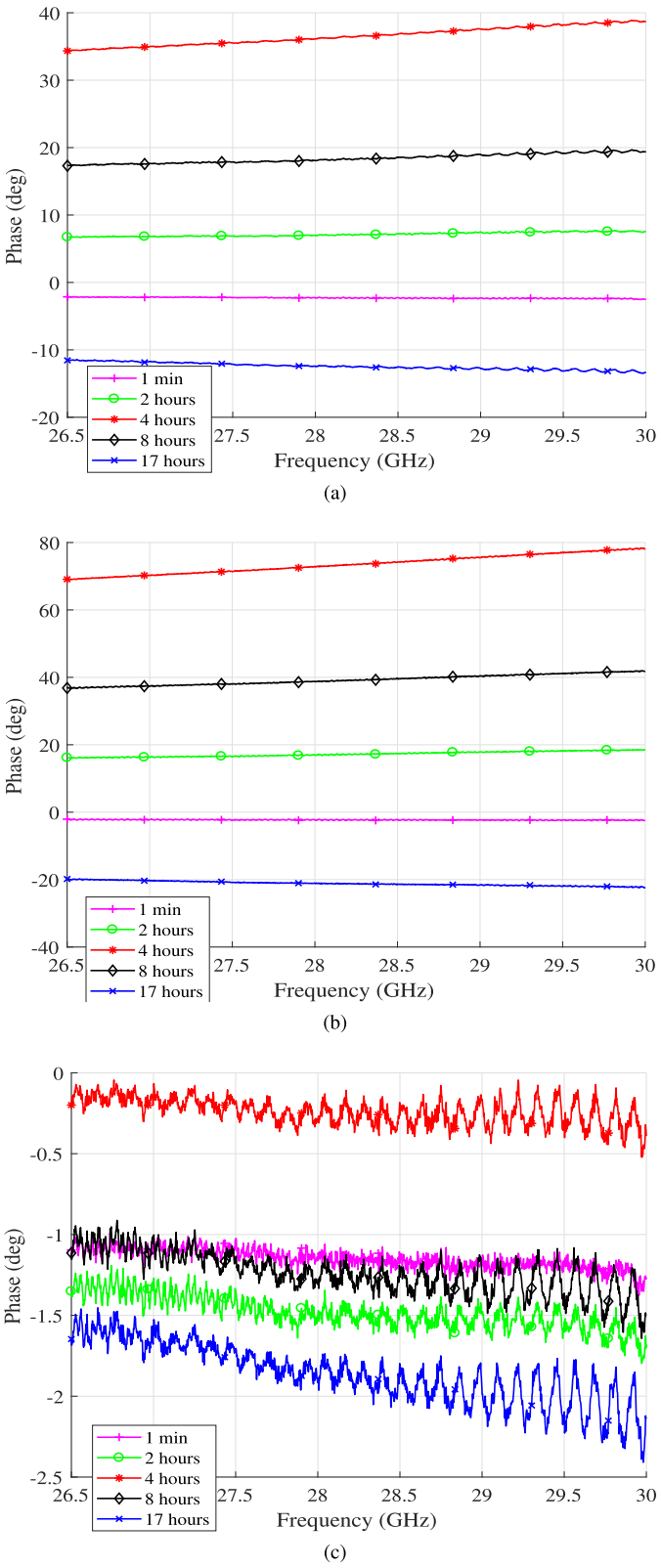

Fig. 6. Unwrapped phase of the channel sounder with the RF amplifier included over a period of 17 h. (a) Phase of the forward link. (b) Phase of the feedback link. (c) Compensated phase.

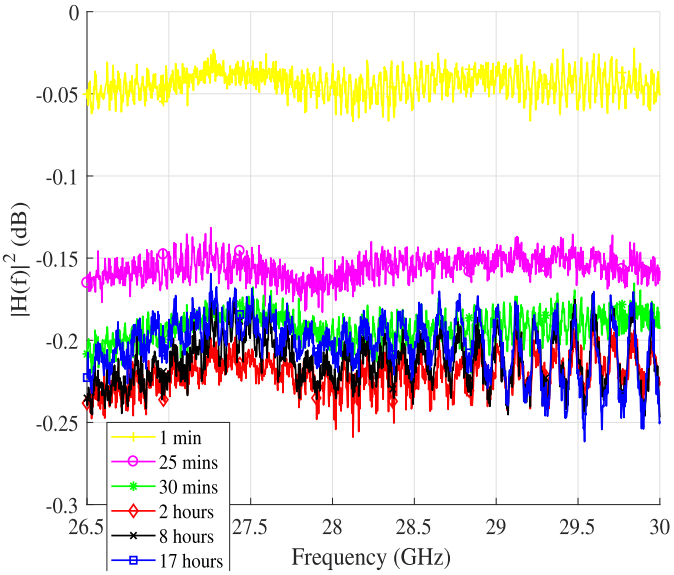

Fig. 7. Amplitude of the channel sounder with the RF amplifier included over a period of 17 h.

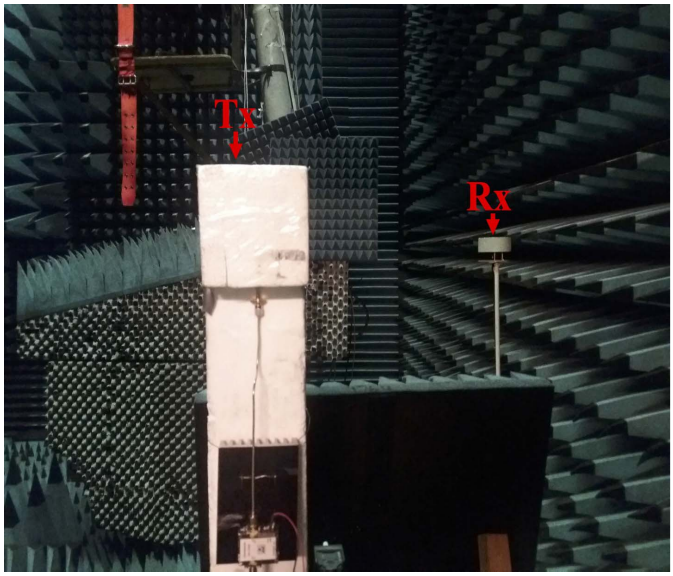

Fig. 8. Anechoic chamber measurement setup.

The phases of the channel coefficients across the different URA elements at a fixed frequency point can be extracted from the measurement data for the LOS component using the space-alternating generalized expectation–maximization (SAGE) algorithm [41]. Specifically, the generic model of the CIR observed at the mth element of the antenna array is formulated as

$$h_m(\tau) = \sum_{\ell=1}^{L} \alpha_{m,\ell}\delta(\tau - \tau_{m,\ell}) + n(\tau) \tag{5}$$

where L represents the path number, $\alpha_{m,l}$ denotes the complex amplitude of the ℓth path, $\tau_{m,\ell}$ is the propagation delay of the ℓth path, $\delta(\cdot)$ denotes the Dirac delta function, and $n(\tau)$ represents the noise. By exploiting the SAGE principle, $\alpha_{m,l}$'s and $\tau_{m,\ell}$'s can be obtained from the measured data for individual array elements. Readers are referred to [41] for the details of the SAGE principle. Since in the anechoic

TABLE II
MEASUREMENT PARAMETERS

Parameter	Value
VNA Tx power	-12 dBm
IF bandwidth	5 KHz
Frequency	26.5 GHz to 30 GHz
Frequency points	6000
Frequency step	583.431 KHz
Sweep time	2.03 s
Tx and Rx antenna height	1.61 m
Virtual URA dimensions	11.6 cm × 11.6 cm

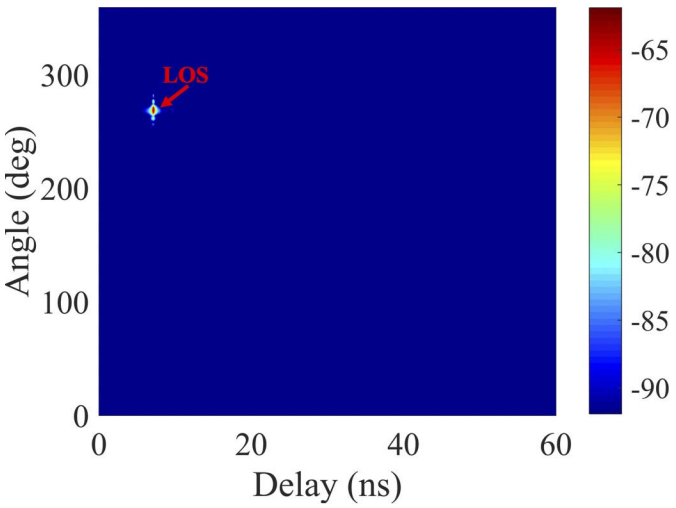

Fig. 9. PADP of the measurement in the anechoic chamber with a dynamic range of 30 dB. The color bar represents power in dB.

chamber, the LOS path is always with the maximum power and minimal propagation delay, the LOS amplitude $\alpha_{m,\mathrm{LOS}}$ and the LOS delay $\tau_{m,\mathrm{LOS}}$ can be easily identified. With the estimated $\alpha_{m,\mathrm{LOS}}$ and $\tau_{m,\mathrm{LOS}}$ values, the channel transfer function at the mth antenna contributed by the LOS path only can be reconstructed as

$$H_m(f) = \alpha_{m,\mathrm{LOS}} \exp(-j2\pi f \tau_{m,\mathrm{LOS}}). \tag{6}$$

Consequently, the phase shift of the LOS path across the array can be obtained by checking the reconstructed channel transfer functions, and the propagation distance can be calculated according to $\tau_{m,\mathrm{LOS}}$'s. The theoretical propagation distance from each antenna element of the virtual URA to the Rx antenna is then compared with the actual measured distance, where a good match is attained as shown in Fig. 10. Fig. 11(a) shows the comparison between the empirical LOS phase shifts and the theoretical LOS phase shifts at 30 GHz across the array. The phase shift across the array can be observed to correspond to the movement of the antenna array positioning stages. The shift to the next y-axis position and the reverse motion along the x-axis can be observed, for example, after the 30th antenna index. The empirical and theoretical phase shifts across the array match well, indicating the robustness of the system. The phase deviation between the

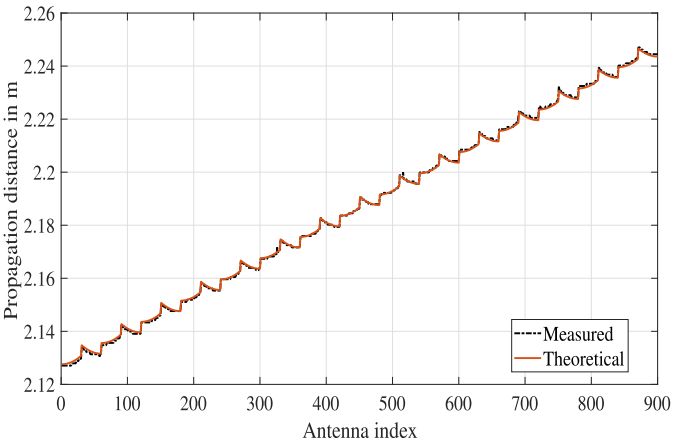

Fig. 10. Theoretical and measured propagation distance from the Tx antenna elements to the Rx antenna. The shape of the plot is as a result of the trajectory of the antenna positioning stages.

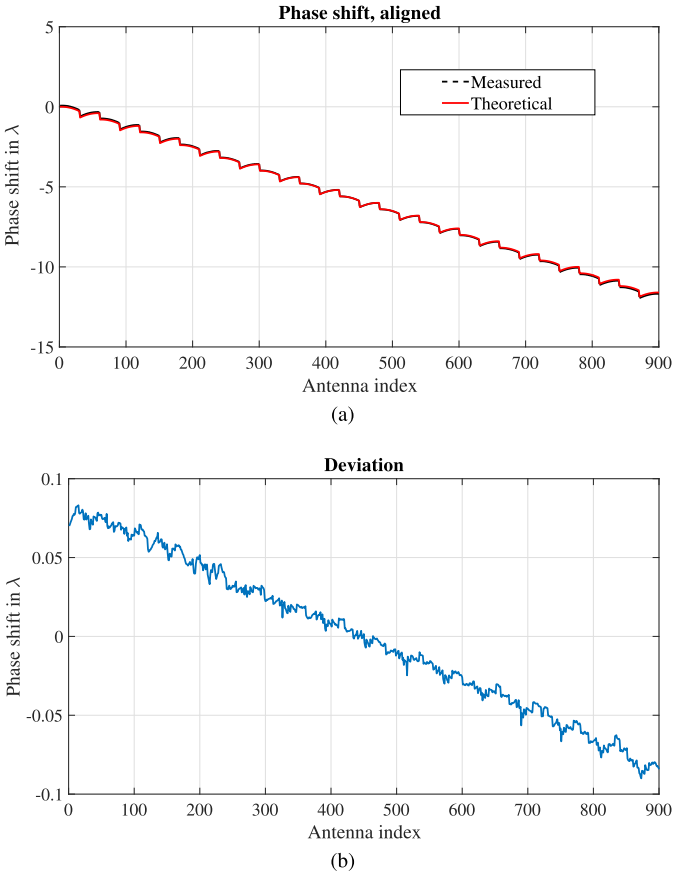

Fig. 11. Phase variation across the virtual URA in wavelength at 30 GHz. (a) Phase shift of the propagating wave from the virtual URA. (b) Phase deviation between the theoretical and measured phase shifts across the virtual URA. The shape of the plots is as a result of the trajectory of the antenna positioning stages.

empirical and theoretical values shown in Fig. 11(b) is most likely introduced by errors in the geometrical alignment of the antennas.

IV. Channel Measurements

A. Measurement Campaigns

Measurement campaigns are carried out in two realistic indoor propagation scenarios in the LOS with the measurement parameters outlined in Table II as follows:

Fig. 12. Short-range indoor measurement with a Tx–Rx separation distance of 5.8 m.

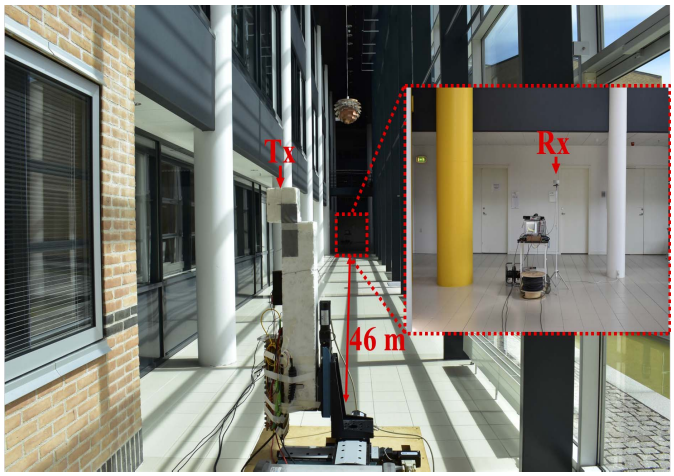

Fig. 13. Long-range indoor measurement with a Tx–Rx separation distance of 46 m in a corridor.

1) short-range measurements in the front of an auditorium;
2) long-range measurements in a corridor environment.

The short-range measurement scenario is shown in Fig. 12. The Tx and Rx antennas are separated by 5.8 m. Behind the Tx antenna, there is a glass window whose curtain had been closed during the measurement. The long-range measurement is carried out in a corridor environment, where the Tx and the Rx are separated by 46 m, as shown in Fig. 13. The placement of the Tx and Rx antennas in relation to the room geometry for the short- and long-range measurement scenarios is shown in Fig. 14. The spatial–temporal response of the channel is then obtained using the Bartlett beamformer, as outlined in [17].

B. Results

In both the short-range and long-range channel measurements, a 40-dB dynamic range is considered relative to the power of the LOS component. In the short-range measurement,

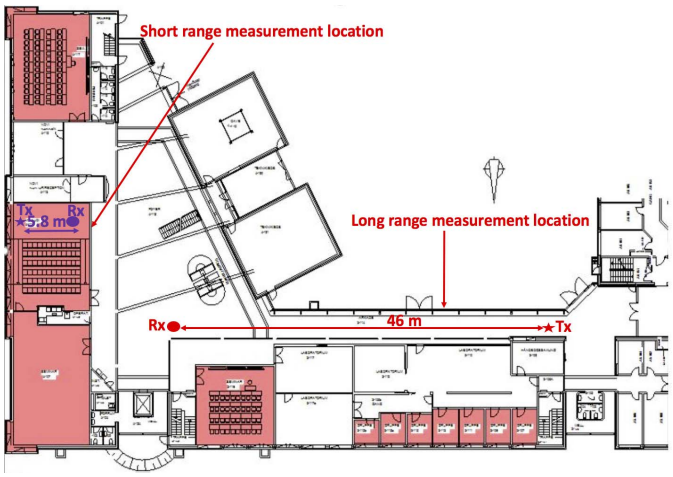

Fig. 14. Placement of the Tx and Rx antennas in relation to the room geometry.

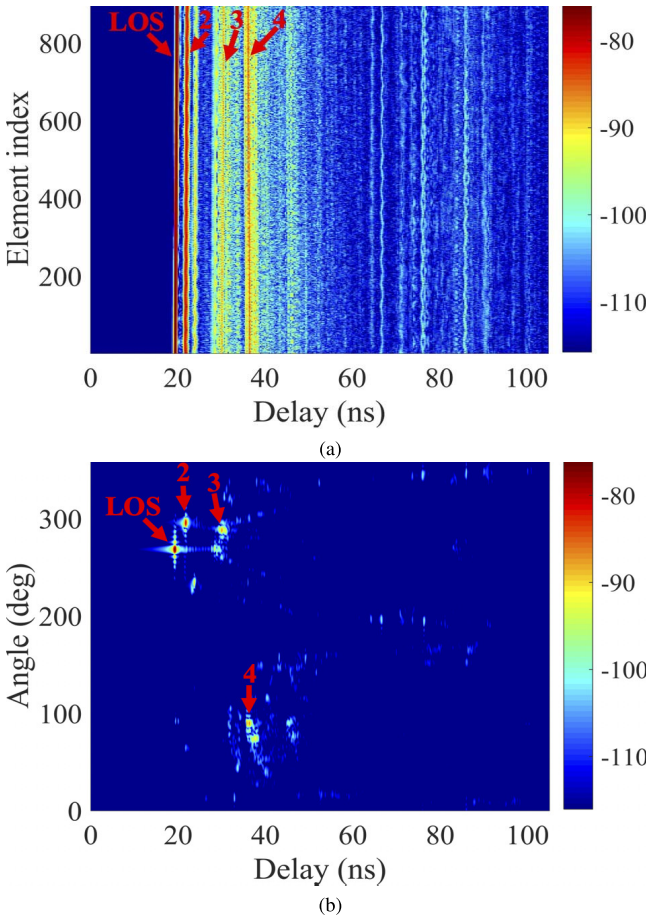

Fig. 15. Short-range indoor channel measurement at a Tx–Rx separation distance is 5.8 m. (a) PDP with a Hanning window applied to suppress the sidelobes and (b) PADP. The color bar represents power in dB.

the PDP of the channel along the URA elements is shown in Fig. 15(a), where the tail of the PDP is observed to decay at around 100 ns. The sparsity of the channel in the angle and delay domains can be observed in the PADP shown in Fig. 15(b). Besides the four dominant paths that have been identified for this analysis, many weak MPCs

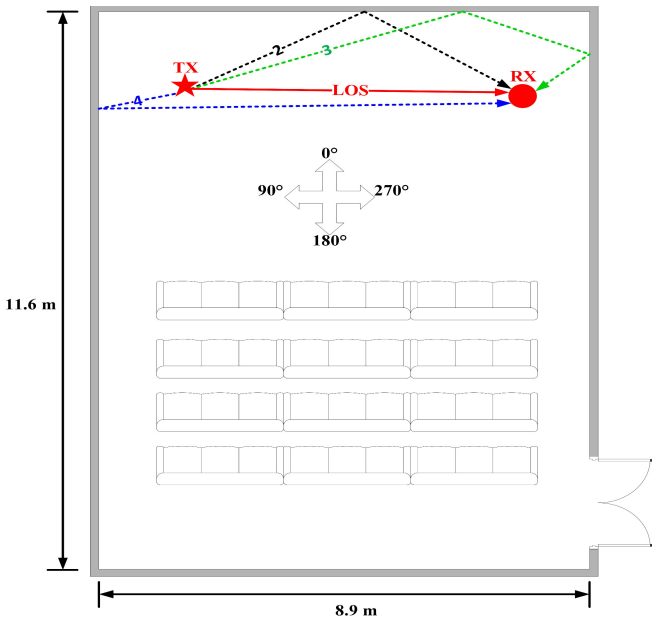

Fig. 16. Relation of the identified MPCs to the room geometry for the short-range channel measurement.

exist, which might be crucial to maintaining the radio link when the LOS component or the dominant MPCs are in blockage.

The LOS has an AoA of 269° and a delay of 19.3 ns, which corresponds to the Tx and Rx antennas' placement and separation distance shown in Fig. 12. The relation of the identified dominant MPCs to the room geometry is shown in Fig. 16. Paths 2 and 3 are MPCs originating from the wall with the blackboard shown in Fig. 12, whereas path 4 is from the curtain behind the Tx antenna. The one-to-one correspondence of the path trajectory and the identified information in the angle and delay domains indicate a good performance of the channel sounder in a realistic propagation scenario.

The PDP of the measurement campaign in the corridor is shown in Fig. 17. Four dominant MPCs are identified, where the last dominant MPC (path 4) has a delay of 654 ns corresponding to a propagation distance of 196 m. The PADP of the long-range measurement is shown in Fig. 18. The LOS component and path 3 have an AoA of 270°, whereas paths 2 and 4 have an AoA of 90°. The mm-wave channel is again observed to be sparse in the angular domain with a few dominant MPCs. Several weak MPCs can also be observed but fade out within 300 ns. It is intuitive to note that two dominant MPCs, paths 3 and 4, come after 500 ns. This observation is fundamental in the design of intersymbol interference mitigation mechanisms in radio networks. The relation of the identified MPCs to the room geometry is shown in Fig. 19. Paths 2–4 are seen to be the first-order, second-order, and third-order reflections, respectively, from the wall behind the Tx and the Rx. The identified angle and delay information corresponds well with the path trajectory, an indication of the channel sounder's performance.

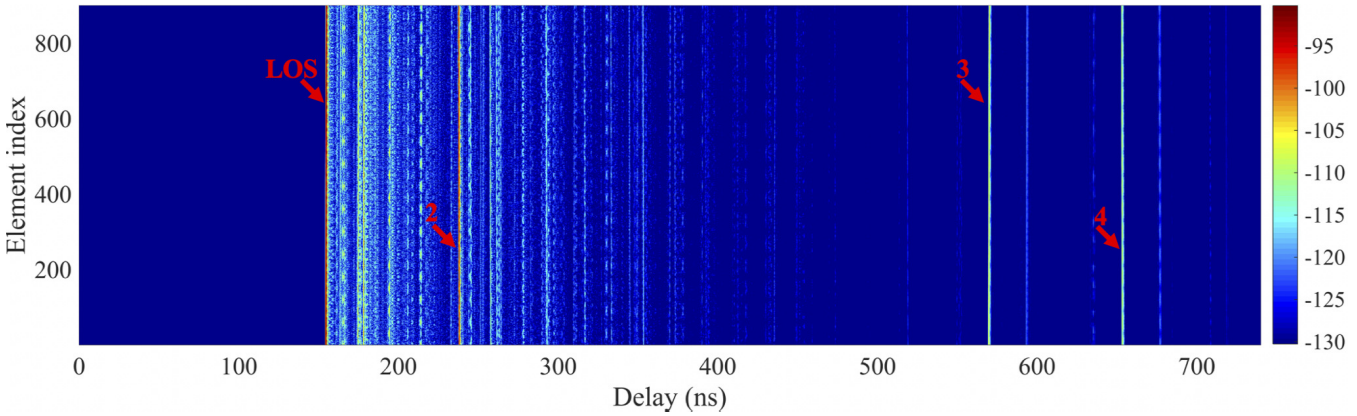

Fig. 17. PDP of the long-range channel measurement with a Tx–Rx separation distance of 46 m. A Hanning window is applied to suppress the sidelobes. The color bar represents power in dB.

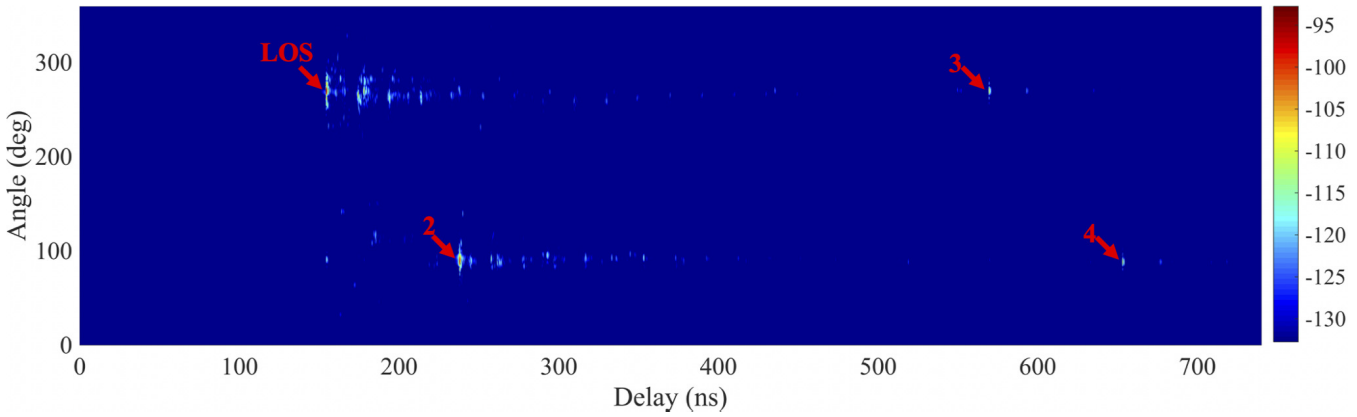

Fig. 18. PADP of the long-range channel measurement with a Tx–Rx separation distance of 46 m. The color bar represents power in dB.

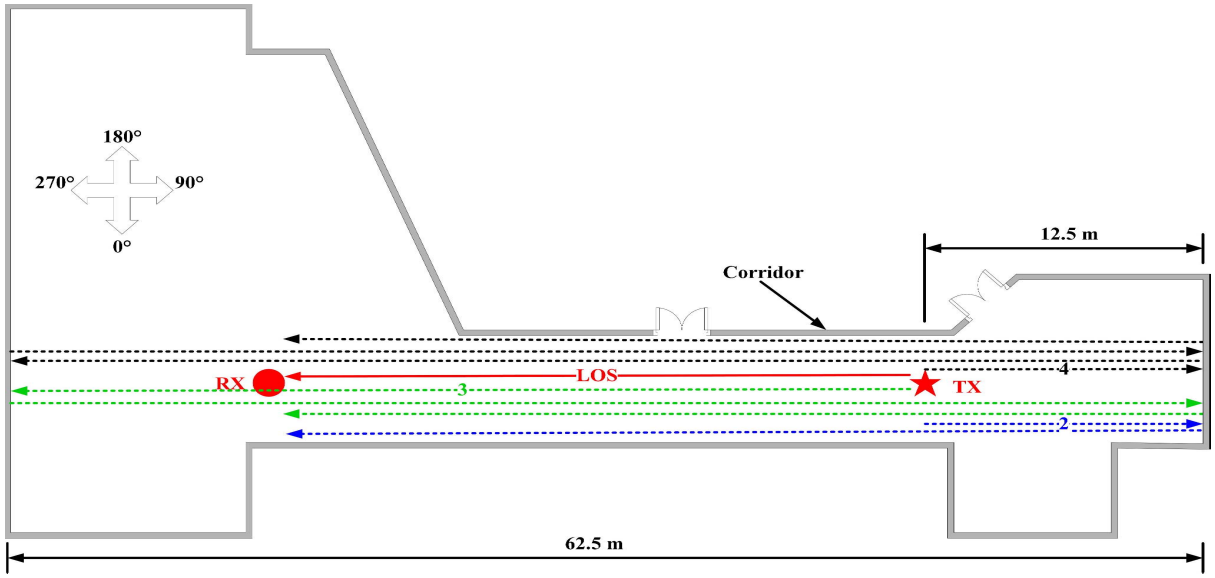

Fig. 19. Relation of the identified MPCs to the room geometry for the long-range channel measurement.

V. Conclusion

In this article, a VNA-based channel sounder using RoF techniques has been presented. The channel sounder is validated and specified for the frequency range of 1–30 GHz for the back-to-back setup and between 26.5 and 30 GHz for the over-the-air measurements due to the limitations imposed by the antennas and the RF amplifier. Using suitable antennas and the RF amplifier, the channel sounder's frequency range can be extended to a maximum of 50 GHz. A novel phase-compensation mechanism using optical circulators is then shown to maintain the phase deviation from normalization to a maximum of 2.5° at 30 GHz. The amplitude stability is also

shown to be robust with a maximum deviation of 0.25 dB over a period of 17 h. In addition to the improvement in the dynamic range to a maximum of 112 dB for the back-to-back connection at 30 GHz, the long- and short-range channel measurements carried out demonstrate the system's high fidelity.

ACKNOWLEDGMENT

The authors would like to thank H. Gao and K. Bank for their help on the measurement setup.

REFERENCES

[1] T. S. Rappaport *et al.*, "Millimeter wave mobile communications for 5G cellular: It will work!" *IEEE Access*, vol. 1, pp. 335–349, May 2013.

[2] J. G. Andrews *et al.*, "What will 5G be?" *IEEE J. Sel. Areas Commun.*, vol. 32, no. 6, pp. 1065–1082, Jun. 2014.

[3] R. He, B. Ai, G. L. Stüber, G. Wang, and Z. Zhong, "Geometrical-based modeling for millimeter-wave MIMO mobile-to-mobile channels," *IEEE Trans. Veh. Technol.*, vol. 67, no. 4, pp. 2848–2863, Apr. 2018.

[4] R. He, B. Ai, G. L. Stüber, and Z. Zhong, "Mobility model-based non-stationary mobile-to-mobile channel modeling," *IEEE Trans. Wireless Commun.*, vol. 17, no. 7, pp. 4388–4400, Jul. 2018.

[5] J. O. Nielsen, W. Fan, P. C. F. Eggers, and G. F. Pedersen, "A channel sounder for massive MIMO and mmWave channels," *IEEE Commun. Mag.*, vol. 56, no. 12, pp. 67–73, Dec. 2018.

[6] G. R. MacCartney and T. S. Rappaport, "A flexible millimeter-wave channel sounder with absolute timing," *IEEE J. Sel. Areas Commun.*, vol. 35, no. 6, pp. 1402–1418, Jun. 2017.

[7] J. Ko *et al.*, "Feasibility study and spatial–temporal characteristics analysis for 28 GHz outdoor wireless channel modelling," *IET Commun.*, vol. 10, no. 17, pp. 2352–2362, 2016.

[8] J. Kivinen, T. O. Korhonen, P. Aikio, R. Gruber, P. Vainikainen, and S.-G. Haggman, "Wideband radio channel measurement system at 2 GHz," *IEEE Trans. Instrum. Meas.*, vol. 48, no. 1, pp. 39–44, Feb. 1999.

[9] J. Kivinen, "60-GHz wideband radio channel sounder," *IEEE Trans. Instrum. Meas.*, vol. 56, no. 5, pp. 1831–1838, Oct. 2007.

[10] R. J. Pirkl and G. D. Durgin, "Optimal sliding correlator channel sounder design," *IEEE Trans. Wireless Commun.*, vol. 7, no. 9, pp. 3488–3497, Sep. 2008.

[11] P. Truffer and P. E. Leuthold, "Wide-band channel sounding at 24 GHz based on a novel fiber-optic synchronization concept," *IEEE Trans. Microw. Theory Techn.*, vol. 49, no. 4, pp. 692–700, Apr. 2001.

[12] T. Zwick, T. J. Beukema, and H. Nam, "Wideband channel sounder with measurements and model for the 60 GHz indoor radio channel," *IEEE Trans. Veh. Technol.*, vol. 54, no. 4, pp. 1266–1277, Jul. 2005.

[13] R. N. Mutagi, "Pseudo noise sequences for engineers," *IEEE Electron. Commun. Eng. J.*, vol. 8, no. 2, pp. 79–87, Apr. 1996.

[14] T. Dammes, W. Endemann, and R. Kays, "Frequency domain channel measurements for wireless localization-practical considerations and effects of the measurement," in *Proc. 18th Eur. Wireless Conf.*, Apr. 2012, pp. 1–8.

[15] D. K. Ghodgaonkar, V. V. Varadan, and V. K. Varadan, "A free-space method for measurement of dielectric constants and loss tangents at microwave frequencies," *IEEE Trans. Instrum. Meas.*, vol. 38, no. 3, pp. 789–793, Jun. 1989.

[16] J. Huang, C.-X. Wang, R. Feng, J. Sun, W. Zhang, and Y. Yang, "Multi-frequency mmWave massive MIMO channel measurements and characterization for 5G wireless communication systems," *IEEE J. Sel. Areas Commun.*, vol. 35, no. 7, pp. 1591–1605, Jul. 2017.

[17] A. W. Mbugua, W. Fan, Y. Ji, and G. F. Pedersen, "Millimeter wave multi-user performance evaluation based on measured channels with virtual antenna array channel sounder," *IEEE Access*, vol. 6, pp. 12318–12326, 2018.

[18] A. Dezfooliyan and A. M. Weiner, "Evaluation of time domain propagation measurements of UWB systems using spread spectrum channel sounding," *IEEE Trans. Antennas Propag.*, vol. 60, no. 10, pp. 4855–4865, Oct. 2012.

[19] P. F. M. Smulders and A. G. Wagemans, "Frequency-domain measurement of the millimeter wave indoor radio channel," *IEEE Trans. Instrum. Meas.*, vol. 44, no. 6, pp. 1017–1022, Dec. 1995.

[20] M. M. Mechaik, "Signal attenuation in transmission lines," in *Proc. IEEE 2nd Int. Symp. Qual. Electron. Design*, Mar. 2001, pp. 191–196.

[21] C. Gentile, S. M. Lopez, and A. Kik, "A comprehensive spatial-temporal channel propagation model for the ultrawideband spectrum 2–8 GHz," *IEEE Trans. Antennas Propag.*, vol. 58, no. 6, pp. 2069–2077, Jun. 2010.

[22] J. Keignart and N. Daniele, "Subnanosecond UWB channel sounding in frequency and temporal domain," in *Proc. IEEE Conf. Ultra Wideband Syst. Technol.*, May 2002, pp. 25–30.

[23] P. Pajusco, N. Malhouroux-Gaffet, and G. E. Zein, "Comprehensive characterization of the double directional UWB residential indoor channel," *IEEE Trans. Antennas Propag.*, vol. 63, no. 3, pp. 1129–1139, Mar. 2015.

[24] J. Hejselbaek, Y. Ji, W. Fan, and G. F. Pedersen, "Channel sounding system for mm-wave bands and characterization of indoor propagation at 28 GHz," *Int. J. Wireless Inf. Netw.*, vol. 24, no. 3, pp. 204–216, 2017, doi: 10.1007/s10776-017-0365-0.

[25] S. Ranvier, M. Kyro, K. Haneda, T. Mustonen, C. Icheln, and P. Vainikainen, "VNA-based wideband 60 GHz MIMO channel sounder with 3-D arrays," in *Proc. IEEE Radio Wireless Symp.*, Jan. 2009, pp. 308–311.

[26] S. Kim, W. T. Khan, A. Zajić, and J. Papapolymerou, "D-band channel measurements and characterization for indoor applications," *IEEE Trans. Antennas Propag.*, vol. 63, no. 7, pp. 3198–3207, Jul. 2015.

[27] S. Priebe, C. Jastrow, M. Jacob, T. Kleine-Ostmann, T. Schrader, and T. Kurner, "Channel and propagation measurements at 300 GHz," *IEEE Trans. Antennas Propag.*, vol. 59, no. 5, pp. 1688–1698, May 2011.

[28] X. Wu *et al.*, "60-GHz millimeter-wave channel measurements and modeling for indoor office environments," *IEEE Trans. Antennas Propag.*, vol. 65, no. 4, pp. 1912–1924, Apr. 2017.

[29] J. Zhu, H. Wang, and W. Hong, "Large-scale fading characteristics of indoor channel at 45-GHz band," *IEEE Antennas Wireless Propag. Lett.*, vol. 14, pp. 735–738, 2015.

[30] A. Kavatjikidis, D. J. Edwards, and C. J. Stevens, "A long-range UWB channel sounding system exploiting UWB over fibre technology," in *Ultra-Wideband, Short Pulse Electromagnetics*. New York, NY, USA: Springer, 2010, pp. 439–447.

[31] J. Medbo, H. Asplund, J.-E. Berg, and N. Jalden, "Directional channel characteristics in elevation and azimuth at an urban macrocell base station," in *Proc. 6th Eur. Conf. Antennas Propag. (EUCAP)*, Mar. 2012, pp. 428–432.

[32] R. Naderpour, J. Vehmas, S. Nguyen, J. Järveläinen, and K. Haneda, "Spatio-temporal channel sounding in a street canyon at 15, 28 and 60 GHz," in *Proc. 27th Int. Symp. Pers. Indoor Mobile Commun. (PIMRC)*, Sep. 2016, pp. 1–6.

[33] W. Stephens and T. Joseph, "System characteristics of direct modulated and externally modulated RF fiber-optic links," *J. Lightw. Technol.*, vol. 5, no. 3, pp. 380–387, Mar. 1987.

[34] M. Calhoun, S. Huang, and R. L. Tjoelker, "Stable photonic links for frequency and time transfer in the deep-space network and antenna arrays," *Proc. IEEE*, vol. 95, no. 10, pp. 1931–1946, Oct. 2007.

[35] F. Zhang, X. Ge, B. Gao, J. Wei, and S. Pan, "Phase stable radio distribution over optic cable by phase conjugation using an optical frequency comb," in *Proc. Int. Top. Meeting Microw. Photon. (MWP)*, Oct. 2015, pp. 1–4.

[36] J. Medbo, H. Asplund, and J. E. Berg, "60 GHz channel directional characterization using extreme size virtual antenna array," in *Proc. IEEE 26th Annu. Int. Symp. Pers., Indoor, Mobile Radio Commun. (PIMRC)*, Aug. 2015, pp. 176–180.

[37] J.-M. Molina-Garcia-Pardo, M. Lienard, and P. Degauque, "Propagation in tunnels: Experimental investigations and channel modeling in a wide frequency band for MIMO applications," *EURASIP J. Wireless Commun. Netw.*, vol. 2009, no. 1, 2009, Art. no. 560571, doi: 10.1155/2009/560571.

[38] W. Fan, A. W. Mbugua, X. Cai, and K. Olesen, "Development and experimental validation of an ultra-wideband channel sounder," in *Proc. 13th Eur. Conf. Antennas Propag. (EuCAP)*, Mar. 2019, pp. 1–5.

[39] J. Li, Y. Zhao, C. Tao, and B. Ai, "System design and calibration for wideband channel sounding with multiple frequency bands," *IEEE Access*, vol. 5, pp. 781–793, Jan. 2017.

[40] S. S. Zhekov, A. Tatomirescu, and G. F. Pedersen, "Antenna for ultrawideband channel sounding," *IEEE Antennas Wireless Propag. Lett.*, vol. 16, pp. 692–695, 2017.

[41] B. H. Fleury, M. Tschudin, R. Heddergott, D. Dahlhaus, and K. I. Pedersen, "Channel parameter estimation in mobile radio environments using the SAGE algorithm," *IEEE J. Sel. Areas Commun.*, vol. 17, no. 3, pp. 434–450, Mar. 1999.

Allan Wainaina Mbugua received the B.Sc. degree in telecommunication and information engineering from the Jomo Kenyatta University of Agriculture and Technology, Juja, Kenya, in 2014, and the M.Sc. degree in telecommunications engineering from the University of Cassino and Southern Lazio, Cassino, Italy, in 2018. He is currently pursuing the Ph.D. degree with the Antennas, Propagation and Millimetre-wave Systems (APMS) Section, Aalborg University, Aalborg, Denmark, with a focus on millimeter-wave radio channel measurements and channel characterization.

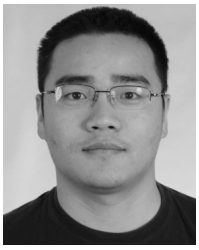

Wei Fan received the B.E. degree from the Harbin Institute of Technology, Harbin, China, in 2009, double master's degrees (Hons.) from the Politecnico di Torino, Turin, Italy, and the Grenoble Institute of Technology, Grenoble, France, in 2011, and the Ph.D. degree from Aalborg University, Aalborg, Denmark, in 2014.

From February 2011 to August 2011, he was with Intel Mobile Communications, Herlev, Denmark, as a Research Intern. He conducted a three-month internship at Anite Telecoms Oy, Oulu, Finland, in 2014. He is currently an Associate Professor with the Antennas, Propagation and Millimetre-wave Systems (APMS) Section, Aalborg University. His current research interests include over-the-air testing of multiple antenna systems, radio channel sounding, modeling, and emulation.

Kim Olesen received the master's degree from Aalborg University, Aalborg, Denmark, in 1988.

He is currently with Aalborg University as the Head of the laboratories with special responsibilities for the Radio and Antenna Laboratory. He has been involved in antenna measurements, channel sounding, massive MIMO and mm-wave measurements, and over-the-air testing of active wireless devices and radio-over-fiber.

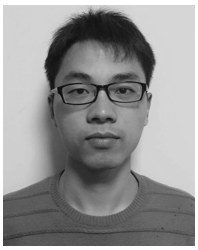

Xuesong Cai received the B.S. and Ph.D. degrees in electronics science and technology from Tongji University, Shanghai, China, in 2013 and 2018, respectively.

He was also a Visiting Scholar with the Universidad Politecnica de Madrid, Madrid, Spain, in 2016. Since May 2018, he has been a Post-Doctoral Fellow with the Antenna, Propagation and Millimeter-wave Systems (APMS) Section, Department of Electronic Systems, Faculty of Engineering and Science, Aalborg University, Aalborg, Denmark. His current research interests include propagation channel measurement, parameter estimation, characterization, and modeling.

Dr. Cai received the National Scholarship for Ph.D. Candidates and the title of Excellent Student in 2016, the title of Excellent Student for the celebration of Tongji University's 110th Anniversary, the ZTE Fantastic Algorithm Award in 2017, and the title of Outstanding Doctorate Graduate awarded by the Shanghai Municipal Education Commission in 2018.

Gert Frølund Pedersen was born in 1965. He received the B.Sc. degree (Hons.) in electrical engineering from the College of Technology in Dublin, Dublin, Ireland, in 1991, and the M.Sc. degree in electrical engineering and the Ph.D. degree from Aalborg University, Aalborg, Denmark, in 1993 and 2003, respectively.

Since 1993, he has been with Aalborg University, where he is currently a Full Professor, heading the Antenna, Propagation and Networking Laboratory with 36 researchers. He is also the Head of the Doctoral School on Wireless Communication with some 100 Ph.D. students enrolled. He was also a Consultant for developments of more than 100 antennas for mobile terminals, including the first internal antenna for mobile phones in 1994 with the lowest SAR, the first internal triple-band antenna in 1998 with low SAR and high TRP and TIS, and lately, various multiantenna systems rated as the most efficient on the market. He has worked most of the time with joint university and industry projects and has received more than $12M in direct research funding. He is the Project Leader of the SAFE project with a total budget of $8M, investigating tunable front end, including tunable antennas for the future multiband mobile phones. He has been one of the pioneers in establishing over-the-air (OTA) measurement systems. The measurement technique is now well established for mobile terminals with single antennas, and he was chairing the various COST groups (swg2.2 of COST 259, 273, and 2100 and now ICT1004) with liaison to 3GPP for OTA test of MIMO terminals. He is currently involved in MIMO OTA measurement. He has published more than 175 peer-reviewed articles and holds 28 patents. His current research interests include radio communication for mobile terminals, especially small antennas, diversity systems, and propagation and biological effects.